metals

MDPI

Article

Dependence of Creep Performance and Microstructure Evolution on Solution Cooling Rate in a Polycrystalline Superalloy

Chao Xu [1,2,3], Feng Liu [1,2,3,*], Lan Huang [1,2,3] and Liang Jiang [1,2,3]

1 State Key Laboratory of Powder Metallurgy, Central South University, Changsha 410083, China; xuchao1994@csu.edu.cn (C.X.); lhuang@csu.edu.cn (L.H.); liang.jiang@csu.edu.cn (L.J.)
2 Powder Metallurgy Research Institute, Central South University, Changsha 410083, China
3 High Temperature Materials Research Institute, Central South University, Changsha 410083, China
* Correspondence: liufeng@csu.edu.cn; Tel.: +86-0731-8883-0938

Received: 30 November 2017; Accepted: 19 December 2017; Published: 22 December 2017

Abstract: It is well known that the solution cooling rate has a great effect on the creep life of superalloys. In this research, three typical cooling rates were applied to generate different distributions of γ′ precipitates for creep tests. Ingots used to make specimens were manufactured by hot extrusion, and the master alloy had the composition of an FGH4096 power metallurgy superalloy. SEM and SESD were used to observe the microstructure's evolution. The experimental results show that the fastest cooling rate corresponds to the highest creep life as well as the smallest rupture strain, and vice versa. The microscopic observations disclose that with an increasing cooling rate, the size and area fraction of γ′ precipitates decrease, and the rupture mechanism changes from transgranular to intergranular. Moreover, some γ′ precipitates changed to cuboid after the creep test. The results will provide new technological processes to design more creep-resistant, nickel-base superalloys.

Keywords: polycrystalline superalloy; creep; rupture; γ′ precipitate

1. Introduction

Polycrystalline nickel-base superalloy is widely used for fabricating the turbine discs of aero-engines, owing to its superior tensile strength, creep resistance and fatigue crack propagation resistance at elevated temperatures [1–4]. These excellent mechanical properties are closely related to the grain-size distribution and γ′ precipitates [5–7]. It is widely accepted that the hub portion typically suffers from higher stress and lower temperatures compared to the rim, leading to tensile strength, low-cycle fatigue cracks and propagation resistance being the main considered factors in designing the microstructure of turbine discs. Recently, turbine-entry temperatures have been further increased, and the in-service working temperature of turbine disc components has been raised accordingly to improve the operation efficiency of jet-engines, resulting in the design optimization of microstructures and mechanical properties [3]. Previous results have documented that creep resistance becomes the paramount concern under higher temperatures, i.e., 700 °C to 900 °C [3,5].

In general, the creep property can be remarkably improved by the optimal heat treatment, which entails controlling the grain size and γ′ precipitates. It is widely reported that the solution's cooling rate governs the attributes of γ′ precipitates [8–12]. A study on the Udimet 500 Ni-base superalloy indicates that size, shape and the area fraction of γ′ precipitates are largely influenced by the cooling rate following partial solution treatments, and the increased cooling rate reinforces alloy strength but decreases ductility [9]. In other research, the morphology and size of γ′ precipitates can be greatly changed by the cooling rate [11,12]. According to Caron, the area fraction of γ′, the precipitate size, the composition and the coherency strains due to the lattice misfit are the four main aspects that

influence creep properties [8]. Bhowal et al. (1990) found a deformation mechanism transition when the inter-spacing of precipitates equals to 50 nm in Rene 95 superalloys [13]. In addition, there are many researchers adopting different cooling rates at the end of solution heat treatments to investigate the interaction between dislocation and γ′ precipitates [14,15].

However, the technological process of powder metallurgy superalloys is long and complicated, which usually includes powder making, hot isostatic pressing (HIP) and isothermal forging (ISF). In this research, we investigate an experimental alloy which has the composition of FGH96 powder metallurgy superalloys, but is made by casting and hot extrusion, a relatively short process. To formulate a better heat treatment scheme, different solution cooling modes are selected to see the influences on the microstructure and creep properties. After the creep test, γ′ precipitates are investigated near the fracture.

2. Experimental Procedures

The master alloy was prepared by vacuum induction melting and cast into an ingot with a diameter of 83 mm. The ingot was then coated with a stainless-steel container and annealed for 8 h at 1100 °C. The hot extrusion temperature was 1100 °C and the reduction area ratio was 4:1. The nominal composition is presented in Table 1.

Table 1. The chemical composition of the superalloy (mass fraction, %).

Cr	Co	W	Mo	Ti	Al	Nb	Fe	Zr	C	B	Ni
15.84	12.59	3.98	3.94	3.73	2.09	0.8	0.093	0.037	0.038	0.012	Bal.

To ensure homogeneity, we found an annular region to manufacture the specimens, and the selected area is marked by red-dashed lines in Figure 1a. The grain of the extruded material is shown in Figure 1b, with the average size measured to be 5.22 μm. The cylinder samples with a size of 11 mm in diameter and 80 mm in length were then cut from the extrusion ingot using electric discharging machining. The heat treatment consisted of solution-based heat treatments and aging treatments. The solution treatment was at 1150 °C for 1 h, followed by three different cooling modes: furnace cooling, air cooling, and oil quenching to room temperature. Finally, all the samples were aged at 780 °C for 8 h, then air cooled to room temperature. During the heat treatment, the temperatures were strictly controlled to be within ±5 °C. To measure the cooling rate, a thermocouple was attached to the specimen to monitor the temperature. The cooling rates were determined by averaging the temperature between the solution temperature and 650 °C.

After the heat treatment, the samples were fine-machined to be 68 mm in total length, 27 mm in gauge length and 5 ± 0.1 mm in diameter. Figure 1c shows the sample drawing. All creep tests were conducted in air at 750 °C/650 MPa to failure. Sample temperatures were controlled with about ±1 °C precision, using three K-type thermocouples in the upper, middle, bottom positions, respectively. After creep tests, the fracture and small slices near the fracture were cut off to observe the microstructure.

The γ′ precipitates were observed by the scanning electron microscope (SEM, Quanta 650, FEI) (FEI, Hillsboro, OR, USA) through a series of mechanical grinding, polishing and chemical etching with a solution of 10 mL H_2O, 10 mL acetic acid, 10 mL HNO_3, and three drops of HF. To remove the residual stress during grinding and polishing, vibration polishing was applied for about 8 h after the standard metallographic procedure for the EBSD (Electron Backscattered Diffraction) observation. A field-emission SEM (FEI, Hillsboro, OR, USA) equipped with an EBSD detector and Channel 5 software (5.11.20405.0, Oxford Instruments, High Wycombe, UK) was used to measure the average grain size.

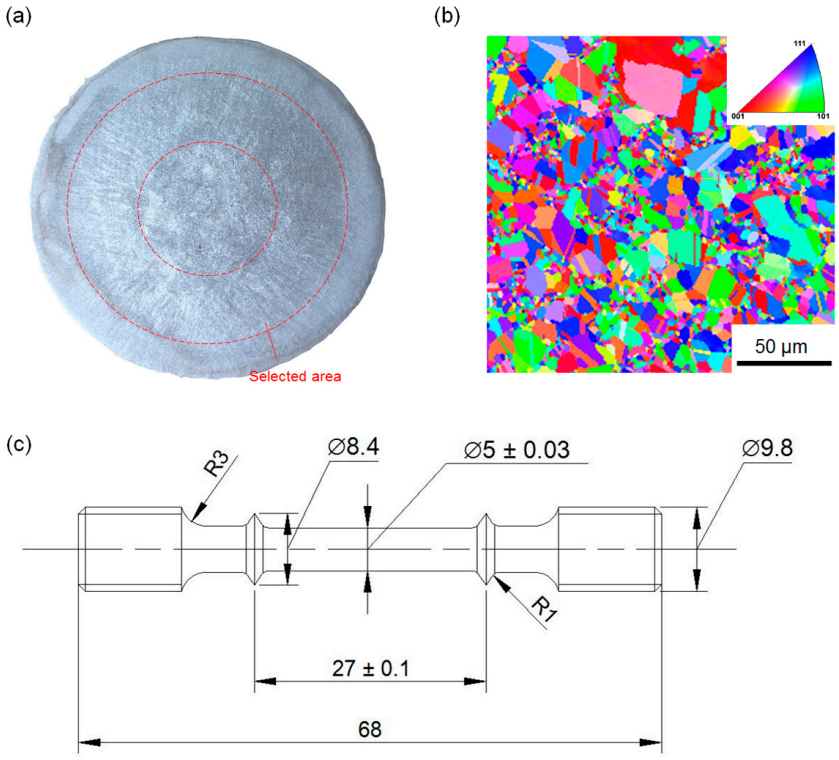

Figure 1. (**a**) Cross section of the extrusion ingot. The annular region between red dashed lines is the selected area to manufacture the specimens; (**b**) Microstructure of the as-extruded material; (**c**) Specimen drawing for creep test (unit: mm).

3. Results and Discussions

Heat treatment is important in the manufacture and repair of gas turbine blades [11]. The purpose of the heat treatment is to optimize the microstructure and its properties in superalloys. The experimental results and discussions that follow are to show the influence of the solution cooling rate on the microstructure and its creep properties.

3.1. Microstructure

Cooling curves and the corresponding γ′ precipitations are presented in Figure 2. It shows that the γ′ precipitates are strongly dependent on the cooling rate. The cooling rate of furnace cooling, air cooling and oil quenching are measured to be 8 °C/min, 307 °C/min and 2029 °C/min, respectively. In the context of furnace cooling, the average size of the γ′ precipitates is calculated to be 185 nm and their morphologies are irregularly-shaped, occasionally presenting butterfly-like features. As the cooling rate is increased, such as air cooling, the average size of the γ′ precipitates decreases to 64.5 nm and their morphologies tend to become spherical, due to more undercooling. When the specimen is oil-quenched, the sizes of γ′ precipitates further decrease and their average value reaches 22.5 nm. The morphologies of γ′ precipitates are nearly-spherical. These results are in good agreement with other studies about the impact of cooling rates on the γ′ precipitation [11,16]. The area fraction of γ′ precipitates, as determined from the micrographs, was 37.7%, 29.7% and 20.7% for furnace cooling, air cooling, and oil quenching, respectively. The relationship between the solution cooling rate and average size as well as the volume fraction of γ′ precipitates are presented in Figure 2b.

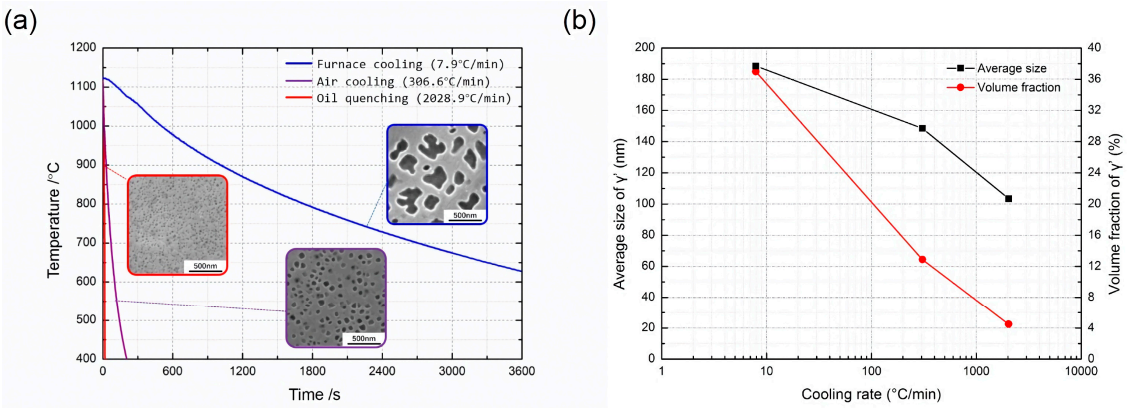

Figure 2. (**a**) Cooling curves of the three different cooling modes. The insets in the frame show typical γ' precipitates after heat treatment; (**b**) Relationship between cooling rate and average size as well as volume fraction of γ' precipitates. Notice that the horizontal axis is logarithmic.

Typical grains are shown in Figure 3. The grain sizes are inhomogeneous, with big grains surrounded by multiple small ones. The statistics show that the average grain sizes are 11.3 µm, 12.2 µm, 11.8 µm for the furnace cooling, air cooling and oil quenching specimens through collecting more than 1000 grains. This indicates that the solution cooling rate has no remarkable influence on the average grain size. We can conclude from the microstructure analysis that after the heat treatments with different solution cooling modes, grain sizes remain unchanged, but the size and area fraction of γ' precipitate change considerably.

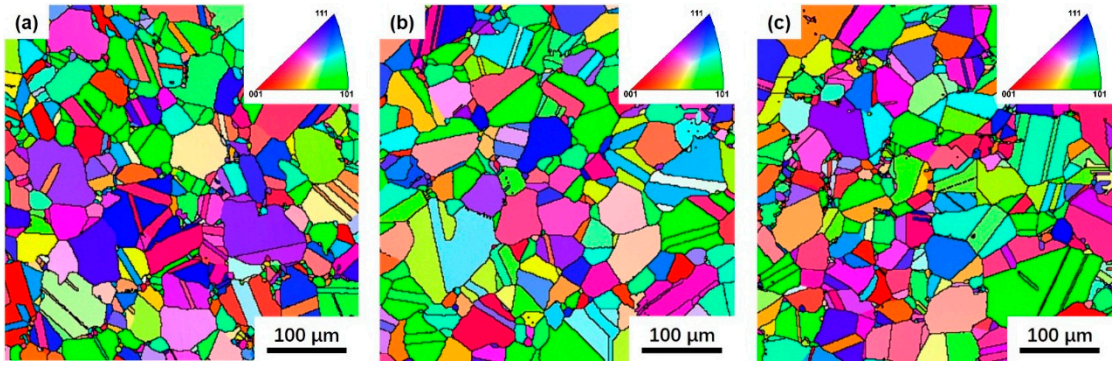

Figure 3. The color map of grains after different heat treatments. (**a**) Furnace cooling; (**b**) Air cooling; (**c**) Oil quenching.

3.2. Creep Results

Based on three types of specimens under different cooling rates, creep tests at 750 °C/650 MPa were carried out to monitor the high-temperature behavior. For each cooling rate, two specimens were tested. Figure 4a shows the creep curves, and it is worth noting that the curves of furnace cooling specimens are not complete. The relationship between cooling rate and the creep life, as well as rupture strain are plotted in Figure 4b. In the case of air cooling and oil quenching, a three-stage creep can be clearly observed in Figure 4a, and the air cooling specimens showed early onset of tertiary creep. In addition, the steady-state creep was short compared to the oil quenching specimens. For the furnace cooling specimens, there were no obvious first and second stages. We can see from Figure 4b that the creep life significantly increased with an increasing cooling rate. The failure life of the oil-quenched specimen exceeds 80 h and the failure strain is less than 1.5%, while the furnace cooling specimen failed within 32 h and the rupture strain observed is more than 7%. Through comparing this data, it is observed that the microstructure of smaller γ' precipitates benefits creep performance.

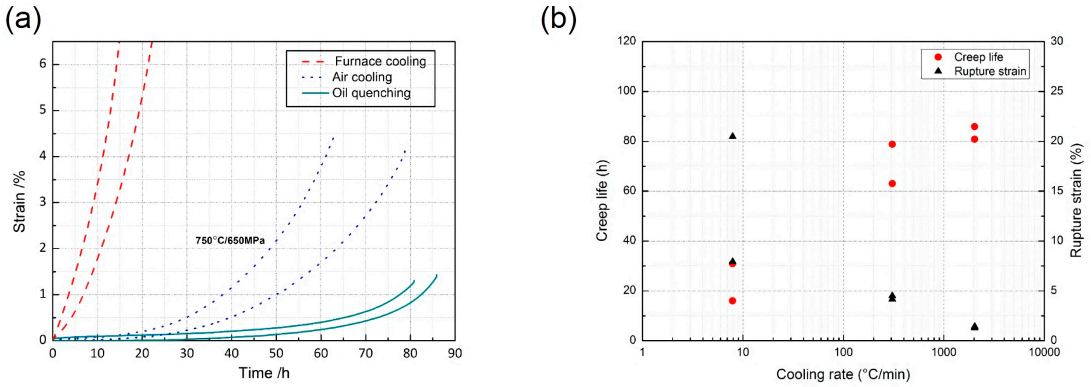

Figure 4. (**a**) Creep curves of alloy with different cooling rates; (**b**) The relationship between cooling rate and creep life as well as rupture strain. Notice that the horizontal axis is logarithmic.

Research on U720 powder metallurgy superalloys reported a creep of 650 °C, as well as reporting that a large γ′ spacing promotes the Orowan mechanism whereas a small γ′ spacing promotes the shearing mechanism; the creep resistance benefits from the shearing mechanism are greater than those of the Orowan mechanism [17], in agreement with the conclusion drawn from another report about an experimental alloy at 700 °C [15].

The shear-stress threshold needed for the Orowan looping may be determined by the following equation [13,18]:

$$\tau_0 = \frac{0.4\mu b}{\pi l_s} \times \frac{\ln(2 \times r_s/b)}{(1-\nu)^{1/2}}.$$

Here, μ is the shear module (72 GPa at 750 °C), b is the Burgers vector (2.54 Å), ν is Poisson's ratio (0.379), r_s is the average radius of γ′ precipitates which can be calculated by $r_s = (2/3)^{1/2} r$, l_s is the mean surface-to-surface spacing of γ′ precipitates and can be determined by the relation:

$$l_s = [(\pi/f)^{1/2} - 2] r_s.$$

The calculated values of r_s, l_s and τ_0 for different cooling modes are shown in Table 2. τ_0 is calculated to be 281.9 MPa, 478 MPa and 726.5 MPa for furnace cooling, air cooling, and oil quenching specimens, respectively. In experiment conditions, the shear stress is about 325 MPa (half of the tensile stress), so only the furnace cooling specimens would promote the Orowan looping. For the air cooling and oil quenching specimens, γ′ shearing may be the main mechanism, thus leading to better creep properties.

Table 2. Threshold shear stress for Orowan looping.

Cooling Mode	r_s/nm	l_s/nm	τ_0/MPa
Furnace Cooling	75.5	67	281.9
Air Cooling	26.3	33	478
Oil Quenching	9.2	17.4	726.5

3.3. Fracture Morphology

Figures 5–7 show the morphology after the creep failure, and indicate that the crack behavior is strongly dependent on the cooling rate. Figure 5 shows the macro appearance of the fractures. Based on different appearances, we divide the macro fracture into the initial region, the propagation region, and the final rupture region. The initial fracture areas can be clearly identified by the color, because they are gravely oxidized compared with other regions. Moreover, cracks are confirmed to initiate along the specimen surfaces. The final rupture area is often convex in shape, where cracks extend

quickly, thus causing rapid failure at the end of the creep test. Between the initial area and the final rupture area is the propagation area which is often a transition region. The three regions are marked in Figure 5, with ① representing the initial fracture area, ② the propagation area and ③ the final rupture area.

We can see that, for the oil quenching specimen, the fracture surface is quite rough, and the surface oxidation is heavy, based on the color change (Figure 5a). In the context of the air cooling specimen, the fracture pathway is macroscopically zigzagged, yet, the fracture is relatively flat and perpendicular to the direction of tension for the oil quenching specimen. More notably, two or more initial regions can be found in the oil quenching specimen (Figure 5c), which are likely to contribute to failure from multiple directions. In addition, based on the SEM observation, the area reduction ratio of furnace cooling, air cooling and oil quenching specimens are 33.8%, 14.5% and 3.5%, respectively. The value of oil quenching specimens is much smaller than that of furnace cooling specimens, indicating a stronger creep resistance.

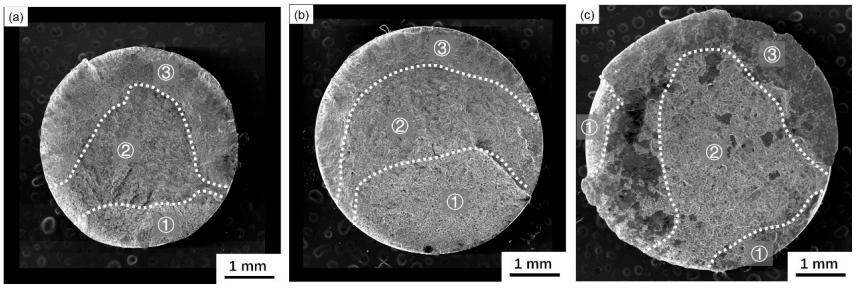

Figure 5. Macro fracture after creep tests. (**a**) Furnace cooling; (**b**) Air cooling; (**c**) Oil quenching. White dotted lines divide the fracture into three areas: ① The initial rupture area; ② The propagation area; ③ The final rupture area.

Figure 6 shows the micro morphology of the initial rupture area, small cracks are found in the furnace cooling specimen, which are marked with white arrows in Figure 6a, and the rugged surface is full of steps. For the air cooling specimen, ubiquitous faceted grains are found at the fracture boundaries (Figure 6b), which is different from the observation in the furnace cooling specimen. Small dimples can be seen on the grain facets (Figure 6e), which means that the fracture is not brittle. For the oil quenching specimen, we can also see small dimples in the initial region, but the grain facets are smoother than the air-cooling specimen, with fewer dimples found in the plane (Figure 6f).

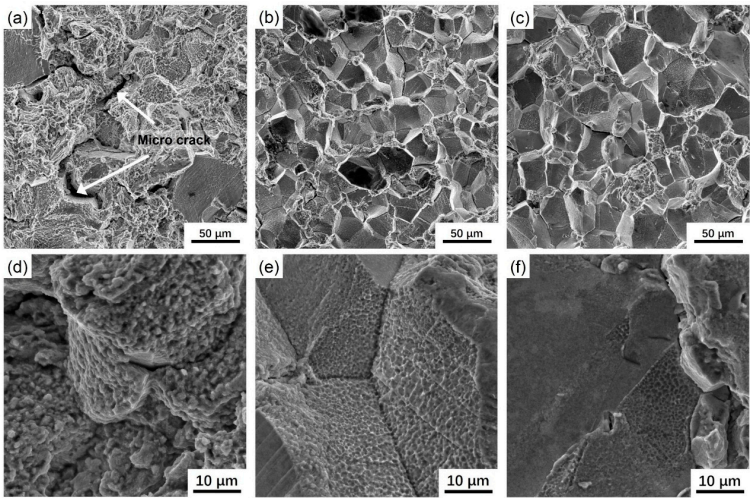

Figure 6. Micro morphology of the initial rupture area. (**a**,**d**) Furnace cooling; (**b**,**e**) Air cooling; (**c**,**f**) Oil quenching. White arrows in (**a**) show the micro cracks.

As for the propagation area shown in Figure 7, dimples and tearing traces are prevalent in all specimens. We can also see some grain facets in the air cooling and oil quenching specimens, but they are heavily deformed (Figure 7b,c). The size of dimples in the oil quenching specimen is smaller than that of dimples in the air cooling specimen (Figure 7e,f), which is probably attributable to the smaller γ′ precipitates in the oil-quenching specimen. For the final rupture region, all specimens exhibit shallow dimples, and there are not many differences between specimens. The microscopic examination indicates that the transgranular cracking is the dominant deformation mode for the furnace cooling specimen, while the intergranular fracture is the primary deformation mechanism for the air cooling specimen, and it becomes more evident that the intergranular crack governs the failure process for the oil quenching specimen. Therefore, we concluded that with the increasing of the solution cooling rate, the rupture mode gradually changed from transgranular to intergranular.

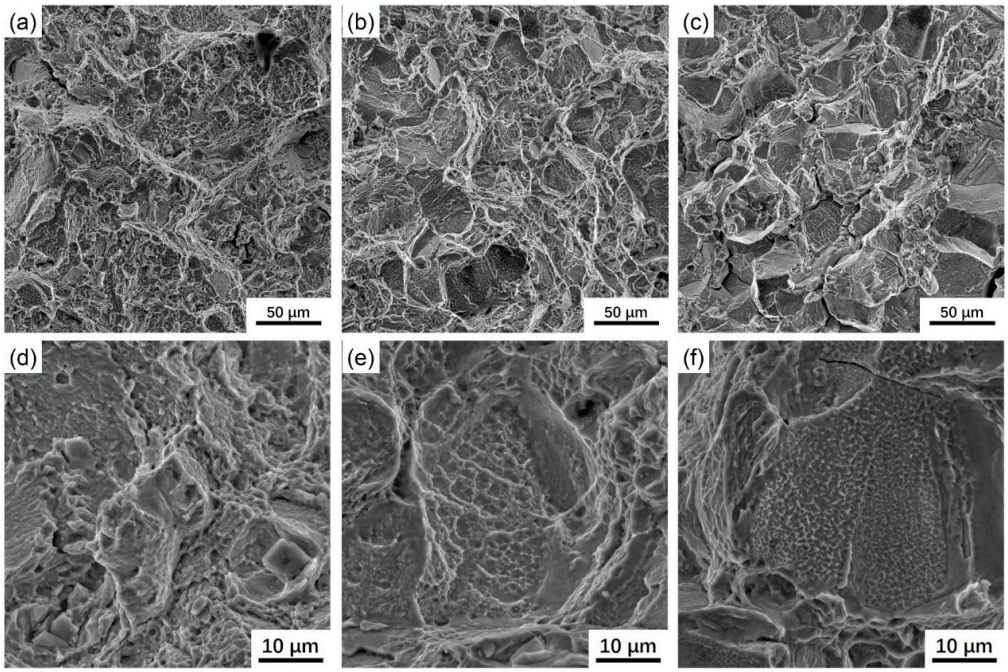

Figure 7. Micro morphology of the propagation area. (**a**,**d**) Furnace cooling; (**b**,**e**) Air cooling; (**c**,**f**) Oil quenching.

3.4. Microstructure after the Creep

After the creep test, a small section of 7 mm, near the fracture, was cut off and split along the load axis for every specimen. Figure 8 demonstrates the microscopic observation of γ′ precipitates at different positions along the gage length. For the furnace cooling specimen (Figure 8a–c) after creep deformation, most γ′ precipitates changed to cuboid from previous irregular-shapes, which is similar to the result of the Ni115 multimodal superalloy after aging for 48 h at 900–1000 °C [19]. This transition is attributed to the coalescence of γ′ precipitates based on the size measurement. According to the observation from three different positions, the area fraction of γ′ precipitates remains stable and implies the absence of temperature and deformation gradients. In the air cooling specimen (Figure 8d–f), a portion of γ′ precipitates have evolved into a cuboid morphology with an increased size due to the particle coalescence. It is noteworthy that the size of finer γ′ precipitates is increased accordingly, but the morphology remains to be pristine. Likewise, the coalescence of γ′ precipitates takes place and the morphology becomes cuboid with a larger size, compared to the air cooling specimen. Noteworthy, the density of large coalesced γ′ precipitates is lower and a dominated percentage of γ′ precipitates exhibit a very small size. In the oil quenching specimen (Figure 8g–i), the area fraction of cuboid γ′ precipitates is lower than in the air cooling specimen, and the remaining spherical γ′ precipitates are

too small to observe from the figure. These particles are so fine that even during long-term aging, they could not grow, nor could their magnitude increase. We can also see from the figure that the size of cuboid γ' precipitates is almost the same for these three specimens.

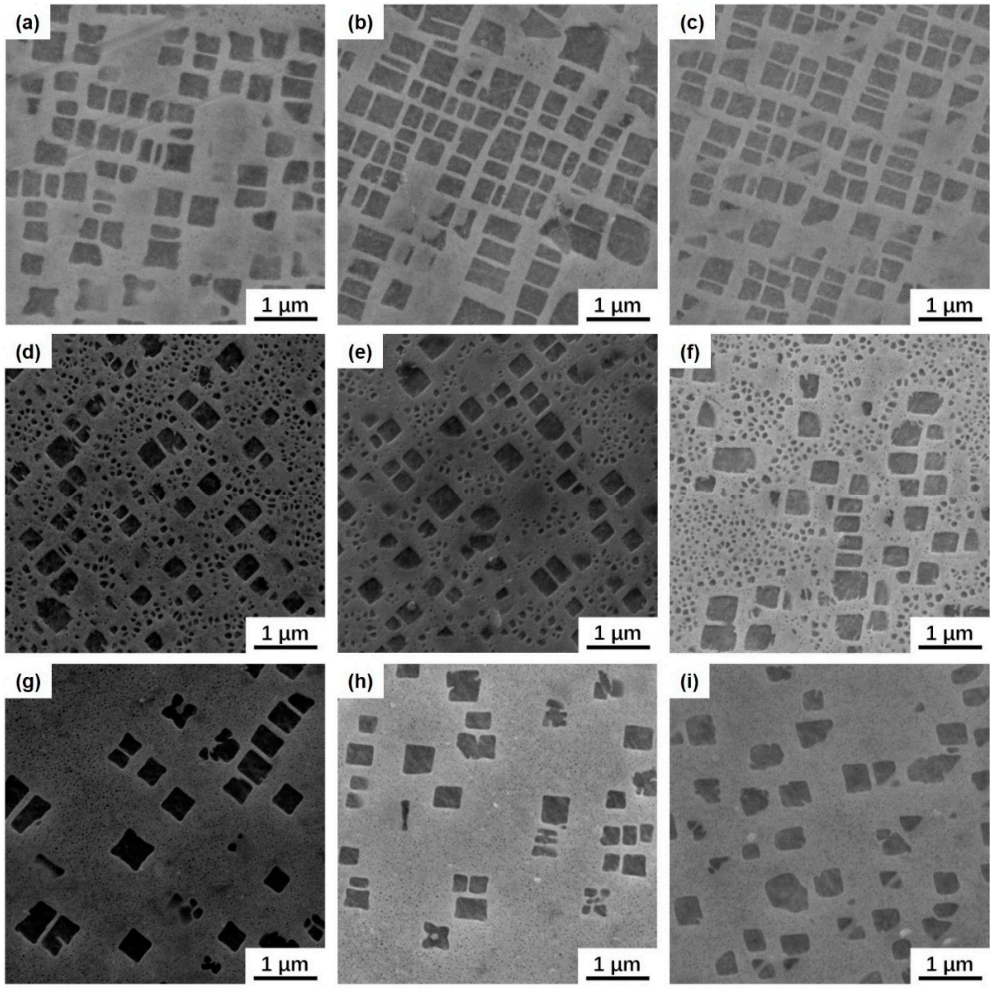

Figure 8. Microstructures near the fracture plane; the plane parallel to the tensile axis is displayed: (**a**–**c**) Furnace cooling; (**d**–**f**) Air cooling; (**g**–**i**) Oil quenching; (**a**,**d**,**g**) About 6 mm away from the fracture plane; (**b**,**e**,**f**) About 3 mm away from the fracture plane; (**c**,**f**,**i**) Near the fracture plane.

Microscopic observation is also carried out on the plane perpendicular to the direction of tension near the fracture surface. Interestingly, in the vicinity of the grain boundaries, a few γ' precipitates approach closely in an aligned manner, which are shown in Figure 9a–c. Figure 9d–f shows the typical microstructures marked with red frames in Figure 9a–c.

For the furnace cooling specimen, a lot of small γ' precipitates are aligned to form the plate-shaped precipitates. For the air cooling specimen, a similar process can be observed (Figure 9b) but the large-sized γ' precipitates become further coalesced and connect in a step-wise way (Figure 9e). The black arrows in Figure 9d,e demonstrate the merging of γ' precipitates. The morphology is like the rafted microstructure observed in a directionally solidified superalloy and single-crystal superalloys, such as CM-247LC and CMSX-4 [3,20]. Few researchers have focused on rafting in polycrystalline superalloys. In one of them, some Co-base superalloys under compression creep conditions have been analyzed, and rafts perpendicular to the load axis have been discovered [21]. A recent study has observed rafting in the Ni-base superalloy IN713LC during the compression creep, but the temperature range used in the creep test was 950–1050 °C [22], which is much higher than the creep temperature in this paper. Rafting formed at intermediate temperatures, i.e., 650–800 °C

and on the tensile load has seldom been reported. A ruptured specimen was discovered after a creep test by Takao Murakumo et al. [23], and a rafted structure perpendicular to the stress axis was observed in the alloys with no more than 60% γ′ precipitates. This finding agrees with our research. That is, rafting is not discovered along the load axis, but observed on the plane perpendicular to the direction of tension. The rafted structure is not observed in the oil quenching specimen. Figure 9f demonstrates the typical feature analogous to Figure 9e, but the grown γ′ precipitates have coalesced into green onion-like aggregates, which ends at the grain boundary. Merging of γ′ precipitates has been discovered before [12,24], but this special morphology has seldom been observed, and the assembly mechanism remains an open question to be investigated. Noteworthy, the density of large coalesced γ′ precipitates is higher near the grain boundary, but lower in the grains, and a dominated percentage of γ′ precipitates still exhibit a small size.

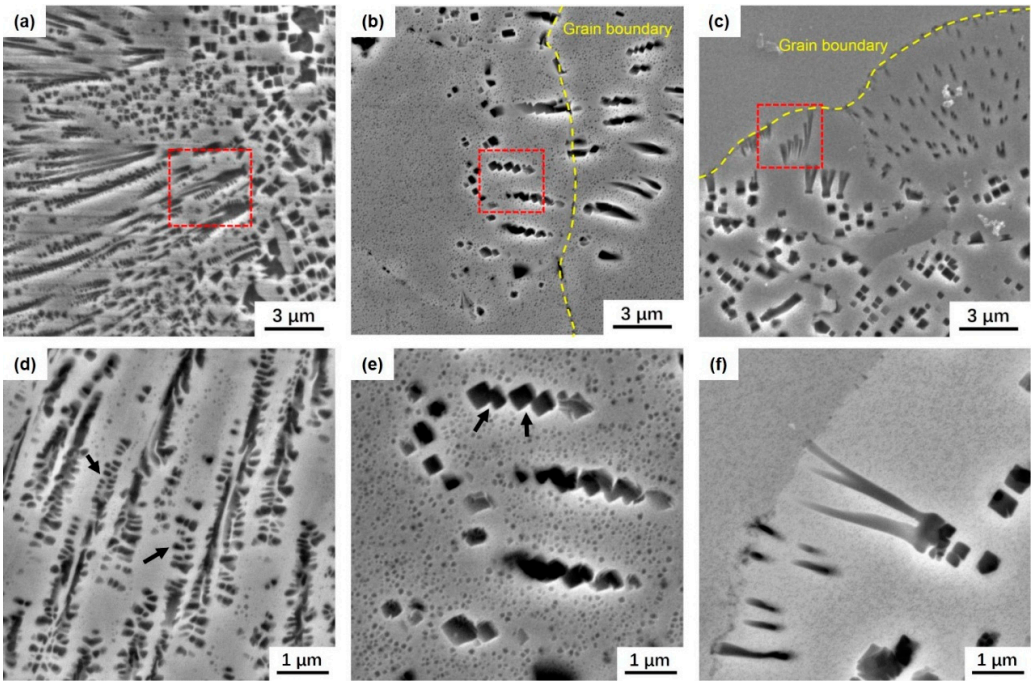

Figure 9. Microstructure of the plane perpendicular to the direction of tension: (**a**,**d**) Furnace cooling; (**b**,**e**) Air cooling; (**c**,**f**) Oil quenching. (**d**–**f**) shows the typical morphology of red frames in (**a**–**c**), respectively.

4. Conclusions

After the supersolvus solution heat treatment, different cooling rates were applied to the superalloys used in this study, in order to examine their influences on microstructure as well as the creep properties. Based on the experimental results, the conclusions may be summarized as follows:

1. The cooling rate of furnace cooling, air cooling and oil quenching is measured to be 8 °C/min, 307 °C/min and 2029 °C/min, respectively. With increasing cooling rates, γ′ size changed from 185 nm to 22.5 nm, the area fraction of γ′ changed from 37.7% to 20.7%, but the grain size remained at about 12 μm.
2. The data of the creep test at 750 °C/650 MPa shows that for the furnace cooling, air cooling, and oil quenching specimens, the mean creep life is 23.45 h, 70.9 h, 83.35 h, respectively. The creep life of the oil quenching specimen is three times longer than that of the furnace cooling specimen. Deformation mechanisms may change from Orowan looping to γ′ shearing as the cooling rates increased. It seems that oil quenching is the best solution cooling mode for the experiment alloy.

3. The rupture mechanism changed from transgranular for the furnace cooling specimen to intergranular for the oil quenching specimen. After the creep test, some γ' precipitates changed to cuboid, and aligned similarly to the rafted structure which is usually observed in single crystal superalloys. Other special γ' merging morphologies were also found. The reason remains to be investigated.

Acknowledgments: Liang Jiang appreciate the financial support from The National Key Research and Development Program of China (2016YFB0701404) and Natural Science Foundation of China (Grant No.:51401242, 51301209).

Author Contributions: Feng Liu, Lan Huang and Liang Jiang conceived and designed the experiments; Chao Xu performed the experiments, analyzed the data and wrote the paper. Hongyu Wu and Xin Wang contributed analysis tools.

Conflicts of Interest: The authors declare no conflict of interest.

References

1. Pollock, T.M.; Tin, S. Nickel-based superalloys for advanced turbine engines: Chemistry, microstructure, and properties. *J. Propuls. Power* **2006**, *22*, 361–374. [CrossRef]
2. Schafrik, R.; Sprague, R. Saga of gas turbine materials. Part IV. *Adv. Mater. Process.* **2004**, *162*, 41–46.
3. Reed, R.C. *The Superalloys: Fundamentals and Applications*; Cambridge University Press: Cambridge, UK, 2008.
4. Zhang, M.; Li, F.; Yuan, Z.; Li, J.; Wang, S. Effect of heat treatment on the micro-indentation behavior of powder metallurgy nickel based superalloy FGH96. *Mater. Des.* **2013**, *49*, 705–715. [CrossRef]
5. Sims, C.T.; Stoloff, N.S.; Hagel, W.C. *Superalloys II*; Wiley: New York, NY, USA, 1987.
6. Torster, F.; Baumeister, G.; Albrecht, J.; Lütjering, G.; Helm, D.; Daeubler, M. Influence of grainsize and heat treatment on the microstructures and mechanical properties of the nickel-base superalloy U720Li. *Mater. Sci. Eng. A* **1997**, *234*, 189–192. [CrossRef]
7. Wei, C.; Bor, H.; Ma, C.; Lee, T. A study of IN-713LC superalloy grain refinement effects on microstructure and tensile properties. *Mater. Chem. Phys.* **2003**, *80*, 89–93. [CrossRef]
8. Caron, P.; Khan, T. Improvement of creep strength in a nickel-base single-crystal superalloy by heat treatment. *Mater. Sci. Eng.* **1983**, *61*, 173–184. [CrossRef]
9. Sajjadi, S.A.; Elahifar, H.; Farhangi, H. Effects of cooling rate on the microstructure and mechanical properties of the Ni-base superalloy UDIMET 500. *J. Alloys Compd.* **2008**, *455*, 215–220. [CrossRef]
10. Khan, T.; Caron, P. Effect of processing conditions and heat treatments on mechanical properties of single-crystal superalloy CMSX-2. *Mater. Sci. Technol.* **1986**, *2*, 486–492. [CrossRef]
11. Safari, J.; Nategh, S. On the heat treatment of Rene-80 nickel-base superalloy. *J. Mater. Process. Technol.* **2006**, *176*, 240–250. [CrossRef]
12. Singh, A.; Nag, S.; Hwang, J.; Viswanathan, G.; Tiley, J.; Srinivasan, R.; Fraser, H.; Banerjee, R. Influence of cooling rate on the development of multiple generations of γ' precipitates in a commercial nickel base superalloy. *Mater. Charact.* **2011**, *62*, 878–886. [CrossRef]
13. Bhowal, P.; Wright, E.; Raymond, E. Effects of cooling rate and γ' morphology on creep and stress-rupture properties of a powder metallurgy superalloy. *Metall. Trans. A* **1990**, *21*, 1709–1717. [CrossRef]
14. Viswanathan, G.; Sarosi, P.; Henry, M.; Whitis, D.; Mills, M. Deformation Mechanisms at Intermediate Creep Temperatures in Rene 88DT. *Superalloys* **2004**, *2004*, 173–178.
15. Kakehi, K. Effect of primary and secondary precipitates on creep strength of Ni-base superalloy single crystals. *Mater. Sci. Eng. A* **2000**, *278*, 135–141. [CrossRef]
16. Laurence, A.; Cormier, J.; Villechaise, P.; Billot, T.; Franchet, J.-M.; Pettinari-Sturmel, F.; Hantcherli, M.; Mompiou, F.; Wessman, A. Impact of the Solution Cooling Rate and of Thermal Aging on the Creep Properties of the New Cast & Wrought René 65 Ni-Based Superalloy. In Proceedings of the 8th International Symposium on Superalloy 718 and Derivative, Marriott Pittsburh City Center, Pittsburgh, PA, USA, 28 September–1 October 2014; John Wiley & Sons: Hoboken, NJ, USA, 2014; p. 33.
17. Goff, S.D.; Couturier, R.; Guétaz, L.; Burlet, H. Effect of the microstructure on the creep behavior of PM Udimet 720 superalloy—Experiments and modeling. *Mater. Sci. Eng. A* **2004**, *387*, 599–603. [CrossRef]

18. Brown, L.M.; Ham, R.K. *Strengthening Mechanisms in Crystals*; Kelly, A., Nicholson, R.B., Eds.; Elsevier: Amsterdam, The Netherlands, 1971; pp. 9–135.
19. Coakley, J.; Basoalto, H.; Dye, D. Coarsening of a multimodal nickel-base superalloy. *Acta Mater.* **2010**, *58*, 4019–4028. [CrossRef]
20. Chiou, M.-S.; Jian, S.-R.; Yeh, A.-C.; Kuo, C.-M.; Juang, J.-Y. High temperature creep properties of directionally solidified CM-247LC Ni-based superalloy. *Mater. Sci. Eng. A* **2016**, *655*, 237–243. [CrossRef]
21. Bauer, A.; Neumeier, S.; Pyczak, F.; Singer, R.; Göken, M. Creep properties of different γ'-strengthened Co-base superalloys. *Mater. Sci. Eng. A* **2012**, *550*, 333–341. [CrossRef]
22. Altincekic, A.; Balikci, E. Precipitate rafting in a polycrystalline superalloy during compression creep. *Metall. Mater. Trans. A* **2014**, *45*, 5923–5936. [CrossRef]
23. Murakumo, T.; Kobayashi, T.; Koizumi, Y.; Harada, H. Creep behavior of Ni-base single-crystal superalloys with various γ' volume fraction. *Acta Mater.* **2004**, *52*, 3737–3744. [CrossRef]
24. Ges, A.; Fornaro, O.; Palacio, H. Coarsening behaviour of a Ni-base superalloy under different heat treatment conditions. *Mater. Sci. Eng. A* **2007**, *458*, 96–100. [CrossRef]